



Article

The Electrochemical Sodiation of Sb Investigated by Operando X-ray Absorption and ^{121}Sb Mössbauer Spectroscopy: What Does One Really Learn?

Ali Darwiche ¹, Marcus Fehse ^{2,3,4} , Abdelfattah Mahmoud ⁵, Camille La Fontaine ⁶, Bernard Fraisse ¹, Raphael P. Hermann ⁷, Marie-Liesse Doublet ^{1,4,8}, Laure Monconduit ^{1,4,8}, Moulay T. Sougrati ^{1,4,8} , Mouna Ben Yahia ^{1,4} and Lorenzo Stievano ^{2,4,8,*}

¹ ICGM, Université de Montpellier, CNRS, 34095 Montpellier, France; ali.darwiche@hotmail.com (A.D.); bernard.fraisse@umontpellier.fr (B.F.); Marie-Liesse.Doublet@umontpellier.fr (M.-L.D.); laure.monconduit@umontpellier.fr (L.M.); moulay-tahar.sougrati@umontpellier.fr (M.T.S.); mouna.ben-yahia@umontpellier.fr (M.B.Y.)

² Dutch-Belgian (DUBBLE), ESRF-The European Synchrotron, 38043 Grenoble, France; marcus.fehse@googlemail.com

³ Faculty of Applied Sciences, Delft University of Technology, 2600 AA Delft, The Netherlands

⁴ Alistore European Research Institute, Université de Picardie Jules Verne, 80039 Amiens, France

⁵ GreenMat, CESAM, Institute of Chemistry B6, University of Liège, 4000 Liège, Belgium; mahmoudrca@gmail.com

⁶ Synchrotron Soleil, Saint-Aubin, 91192 Gif-sur-Yvette, France; camille.lafontaine@synchrotron-soleil.fr

⁷ Materials Science and Technology Division, Oak Ridge National Laboratory, Oak Ridge, TN 37813, USA; hermannrp@ornl.gov

⁸ Reseau sur le Stockage Electrochimique de l'Energie (RS2E), CNRS, 80039 Amiens, France

* Correspondence: lorenzo.stievano@umontpellier.fr; Tel.: +33-467-143346

Received: 4 May 2018; Accepted: 28 May 2018; Published: 30 May 2018



Abstract: In this study, we want to highlight the assets and restrictions of X-ray absorption spectroscopy (XAS) and Mössbauer spectroscopy for investigating the mechanism of the electrochemical reaction of antimony electrode materials vs. Na. For this, *operando* XAS was carried out during the first one and a half cycles, and the whole set of measured data was analysed using a statistical-chemometric approach, while low temperature Mössbauer spectroscopy measurements were carried out *ex situ* on selected samples stopped at different points of the electrochemical reaction. Complementary ab initio calculations were performed to support the experimental findings. Both techniques show that, upon the first sodiation, most Sb reacts with Na to form disordered Na_3Sb . This step is accompanied by the formation of amorphous Sb as an intermediate. Upon inversion of the current Na_3Sb is desodiated and an amorphous Sb phase, distinct from the pristine bulk Sb state, is gradually formed. However, both XAS and Mössbauer spectroscopy were unable to spot the formation of intermediate Na_xSb phases, which were evinced in previous works by *operando* Pair Distribution Function analyses. The results shown here clearly assign such failure to the intrinsic inability of both techniques to identify these intermediates.

Keywords: X-ray absorption spectroscopy; Mössbauer spectroscopy; DFT calculations; chemometrics; MCR-ALS; Na-ion batteries; alloy reaction; Sb

1. Introduction

In the last decades, a strong expansion of the application of energy storage systems based on Li-ion batteries has been observed, going from the fields of portable devices and electric vehicles to

the storage of the energy produced by intermittent renewable energy sources. However, the strong localisation of the lithium-rich resources on earth might strongly influence the price and the availability of lithium in the long term [1]. In such a picture, sodium-ion batteries (NIB) are of great interest to serve as backbone for some of the proposed applications, such as those concerning renewable energies, due the abundance, worldwide distribution and low-cost of raw materials. In particular, NIB could be an economically viable alternative to Li-based systems for large-scale systems (e.g., grid storage) because of the greater abundance and lower cost of sodium-containing precursors [2,3]. Among the possible negative electrode materials, antimony was recently shown to be a viable negative electrode material for NIB due to its high theoretical capacity of 660 mAh g^{-1} (corresponding to the formation of Na_3Sb), its high electrical conductivity and very good cyclability vs. Na in spite of the huge observed volume expansion upon sodiation [4].

In a pioneer study, we showed that the sodiation of antimony offers high capacity and reasonable capacity retention [5]. Furthermore, we highlighted that the sodiation process differs significantly from lithiation, in spite of identical starting materials and similar phases at the end of discharge $M_3\text{Sb}$ ($M = \text{Na}$ or Li). While the lithiation process occurs on a single long slope, the sodiation reaction mechanism involves at least three processes which indicate complex multistep reaction and intermediate formation. These mechanistic differences have profound implications on capacity retention and cycle life. Due to much stronger amorphization during the sodiation process the formation of an Na_xSb ($x \approx 1.5$) intermediate could only be postulated but not evidenced in that study, which was mainly based on X-ray diffraction (XRD) analyses.

In a recent work, however, phase diagram calculations made by our group have pointed out the existence of Na_xSb phases close to the two-phase reactions ($\text{Sb} \rightarrow \text{NaSb} \rightarrow \text{Na}_3\text{Sb}$) confirming the complexity of sodiation mechanism [6]. Moreover, short-range probing spectroscopic techniques such as *operando* Pair Distribution Function (PDF) and *ex situ* ^{23}Na Solid State Nuclear Magnetic Resonance (NMR) were applied in a subsequent study to investigate the formation of intermediates upon sodiation of Sb [7]. In the latter study, two new intermediates were identified, namely $\text{Na}_{\approx 1.7}\text{Sb}$ and Na_{3-x}Sb , which underpins distinction of sodiation from lithiation process but also demonstrates the usefulness of short-range spectroscopic techniques for gaining in-depth information on complex electrode reactions.

The latter work completes and clarifies the mechanisms previously proposed by Baggetto et al. [8,9] who also suggested the possible formation of amorphous Na_xSb phases with a composition similar to NaSb mostly based on a non-unique hypothetical deconvolution of the ^{121}Sb Mössbauer spectra measured along the sodiation/desodiation line.

In this new study, we would like to, on the one hand further improve the understanding of the sodiation/desodiation processes in antimony with the help of two short-range probing techniques such as XAS and Mössbauer spectroscopy, and on the other demonstrate that the extent of the information that can be gained throughout these two techniques is unfortunately only limited. In particular, with the help of DFT calculations, we will show that in the specific case of Sb vs. Na part of this information remains concealed due to intrinsic properties of the probing techniques.

2. Experimental

2.1. Materials

The micrometric powder of antimony used in this study was provided by Alfa-Aesar (99.5% purity, ≈ 325 mesh) and was used without any additional treatment. NaSb and Na_3Sb intermetallics were prepared by ball milling stoichiometric mixtures of Sb and sodium metal (Sigma Aldrich, St. Louis, MO, USA, 99 %) using a Retsch PM 100 planetary ball mill. The metals were loaded into a 50 ml air-proof hardened stainless steel jar under Ar atmosphere with 6 steel balls (5 g each). An active-milling time of 60 min was enough to obtain a complete reaction of Sb and Na, which is notably faster and easier than

the classical synthesis by heating at temperatures exceeding the melting points (650 °C and 906–956 °C for NaSb and Na₃Sb) [10,11].

Sb electrodes containing 70 wt % active material were prepared using a mixture of carbon black and vapor ground carbon fibers (VGCF-S) as the conductive additive (15 wt %), and carboxymethyl cellulose (CMC) as the binder (15 wt %) as described in detail elsewhere [5]. Standard coin cells were assembled in an argon-filled glove-box to test the electrochemical performance of the prepared electrodes against a metallic sodium counter-electrode. The electrolyte was made of 1 M NaClO₄ in PC with addition of 5% fluoroethylene carbonate (FEC). A disc of Whatman glass fiber was used as the separator. All tests were carried out at C/20, corresponding to the reaction of one mole of Na per mole of Sb in 20 h, using a multichannel VMP system under galvanostatic conditions.

2.2. Methods

XRD analyses were performed with a X'Pert Pro diffractometer with the Cu K_α radiation. Samples were protected using a Kapton film to avoid any contact with air and to prevent their decomposition. The crystallographic cell parameters of the reference phases were refined using FULLPROF software [12].

The ¹²¹Sb Mössbauer spectra were measured with a 0.4 mCi source of ^{121m}Sn in a matrix of CaSnO₃. The measurements were performed with the source at ambient temperature and the sample at 78 K with a triangular velocity waveform in the classical transmission geometry using a closed-circuit helium cryostat (Janis SH-850). A LiF scintillation detector was used for the detection of the γ -rays. The samples with a Sb loading of about 10 mg cm⁻² were placed in sealed thin-walled PMMA containers to prevent their decomposition. The Mössbauer spectra were fitted by using the PC-Mos II computer program with appropriate superpositions of Lorentzian lines [13]. The relative intensities and positions of the eight individual lines expected for an electric quadrupole pattern in the case of the 5/2 → 7/2 M1 transition of ¹²¹Sb were calculated from the appropriate Clebsch-Gordan coefficients and the Hamiltonian for a pure axially symmetric quadrupole interaction, respectively. In this way, spectral parameters such as the isomer shift (δ), the electric quadrupole splitting (Δ), the asymmetry parameter (η), the experiment full line width at half maximum (Γ) and the relative resonance areas (Area) of the different components of the absorption patterns were determined. It is worth noting that the quadrupole splitting Δ really corresponds to e^2qQ of the 5/2+ ground state of ¹²¹Sb, where eq is the electric field gradient and Q the quadrupole moment. The results of the fit of the Mössbauer spectra measured at 78 K are reported in Tables 1 and 5 for the reference compounds and the cycled electrodes, respectively. The isomer shifts are referred to the CaSnO₃ source.

XAS measurements at the Sb K-edge were performed in the transmission mode at the SAMBA beamline of Synchrotron SOLEIL in Gif-sur-Yvette (France). A Si(220) double crystal monochromator with an energy resolution of 1 eV at 30 keV was used. The intensity of the monochromatic X-ray beam was measured by three consecutive ionization detectors. The in situ electrochemical cell [14] was placed between the first and the second ionisation chambers, and the homogeneity of the sample was checked before running the electrochemical test. The latter was carried on continuously for the first cycle and a half (discharge/charge/discharge). The electrochemical signature of the in situ cell and the correspondence with the *operando* spectra is reported in the Supplementary Materials.

In the XANES (X-ray absorption near-edge structure) region of Sb K-edge (30,491 eV), equidistant energy steps of $E = 1$ eV were used. For all measured spectra, the exact energy calibration was established with simultaneous absorption measurements on a Sb metal foil placed between the second and the third ionisation chamber. The first inflection point of the XAS pattern of Sb (30,491 eV) was used for the energy calibration. The absolute energy reproducibility of the measured spectra was ± 0.1 eV.

EXAFS (Extended X-ray Absorption Fine Structure) spectra were collected up to $k = 16 \text{ \AA}^{-1}$. The spectra of the pure reference compounds (Sb, NaSb and Na₃Sb) were extracted and fitted using the Demeter software package [15]. Fourier transform of EXAFS oscillations with different k weights

was carried out in k -range from 3.0 to 13.0 \AA^{-1} . Fitting was performed in R range from 1.5 to 5 \AA using k^2 and k^3 weights. EXAFS amplitudes and phase-shifts were calculated using the program FEFF7 [16] starting from the calculated lattice parameters of NaSb and Na₃Sb and Sb metal (vide infra). The amplitude reduction factor S_0^2 was fitted in the spectrum of Sb metal, used as an internal standard, to the value of 0.98. In the fitting of the other spectra, S_0^2 was kept fixed to this value. In the case of spectra containing signal originating from multiple phases, the sum of the S_0^2 of each phase was made equal to 0.98. Coordination numbers N were kept fixed during the fitting, whereas interatomic distances (R) and the Debye-Waller factors (σ^2) were calculated for all paths included in the fits. These parameters are reported in Table 3.

The *operando* EXAFS spectra were first globally analysed using a statistical tool named Principal Component Analysis (PCA) using the computer program Matlab [17]. PCA is a chemometric factor analysis tool, and is generally used to discover the minimal particular structures in multivariate spectral data sets. More precisely, it is used here to determine the number of independent components contributing to the whole series of collected spectra during electrochemical cycling. The number of principal components determined in this way was used as the basis for Multivariate Curve Resolution-Alternating Least Squares (MCR-ALS) analysis [18,19]. This algorithm allows the stepwise reconstruction of the spectral components which are necessary for interpreting the whole multiset of *operando* spectra. The MCR-ALS analysis was performed with the following constraints: (i) non-negativity of the intensity of the components, (ii) unimodality for one of the three components and (iii) closure (sum of the 3 components always equal to 100 % of the intensity). The reconstructed spectral components were then fitted using the IFEFFIT software package in the same way as for the reference compounds. The fitting parameters are reported in Table 4, while the fitted components are shown in the Supplementary Materials together with the corresponding goodness of fit parameter R .

2.3. Theoretical Calculations

First-principles Density Functional Theory (DFT) calculations including full structural relaxations were performed using B3LYP exchange and correlation as implemented in the ab initio CRYSTAL14 code [20–23]. All-electron description was included through the use of the 8-511G and 9763111-631G basis sets on Na and Sb. A total number of k-points of 65, 133 and 268 were needed to correctly describe the irreducible Brillouin zone of Sb, NaSb and Na₃Sb, respectively.

The Mössbauer spectral parameters are then evaluated on relaxed structures using a calibration procedure. The hyperfine constants appraised from DFT are known to be sensitive to the type of functional and basis set used for the calculation, in relation with the problem of universality in the description of the electron density at the nucleus. However, robust experimental and theoretical correlation were previously reported using DFT approach at wide series of solid compounds and parameters like isomer shift and quadrupole splitting are well determined [24–26]. The calibration procedure consists in firstly estimating the (α) slope correlated to the nuclear transition and the ρ_0 referred to the electron contact density of the source CaSnO₃ in $\delta = \alpha(\rho - \rho_0)$ equation, by plotting the calculated nuclear charge density at the nuclear position ρ (electron contact density) of several reference Sb compounds (listed in Supplementary Materials) versus their experimental isomer shift values δ . Then, from the calibration line, the calculated electron contact density of any Na_xSb phase leads to the evaluation of related isomer shift. The quadrupole splitting was inferred through the same scheme and using the same set of compounds. Simulation of electric-field gradient component along z (V_{zz}) of several solids containing Sb, compared to the measured quadrupole coupling constant (Δ) allows calculating the value of the nuclear quadrupole moment Q deriving from the relation $\Delta = 1/2eV_{zz}Q(1 + \eta^2/3)^{1/2}$. This linear correlation allows interpolating the quadrupole splitting of the Na_xSb compounds knowing their calculated V_{zz} . The simulated hyperfine parameters are reported in Table 2 and more details on calibration procedure are shown in Figure S3 and in the Supplementary Materials.

3. Results

3.1. Pure Sb and Na-Sb Intermetallics

The structures of pure antimony and of the two known Na-Sb intermetallics (i.e., NaSb and hexagonal Na₃Sb) are shown in Figure 1 together with their respective experimental XAS and ¹²¹Sb Mössbauer spectroscopy signatures. The XRD patterns (see Supplementary Materials) were successfully refined in the expected *P63/mmc* (cell parameters $a=b=5.35(6)$ Å, and $c=9.49(2)$ Å) and *P21/c* (cell parameters $a=6.78(7)$ Å, $b=6.33(6)$ Å, $c=12.47(2)$ Å and $\beta=117.51(4)^\circ$) space groups for Na₃Sb and NaSb, respectively, in very good agreement with the structures reported in the Na-Sb phase diagram and with previous reported theoretical calculations [6,10,27,28].

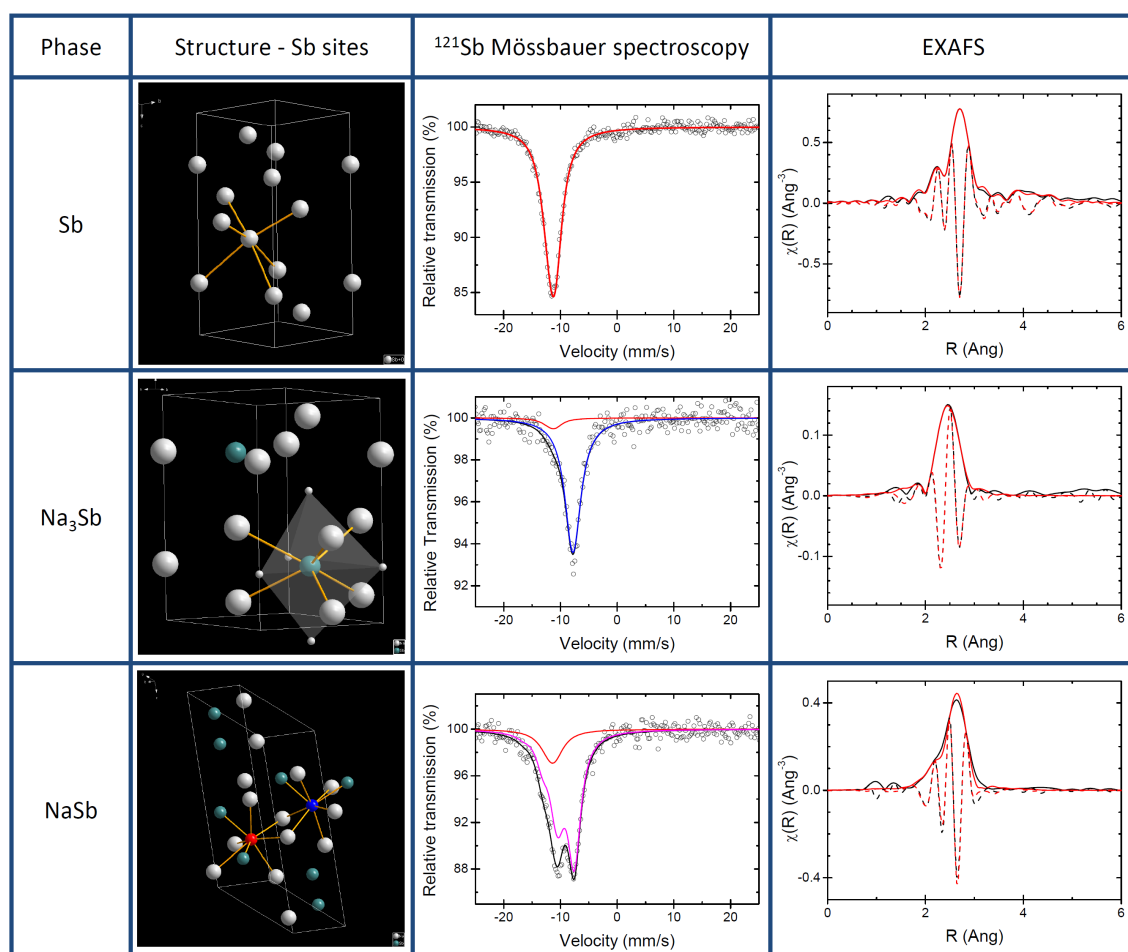


Figure 1. From (left) to (right): Local coordination of the Sb centres, ¹²¹Sb Mössbauer and EXAFS spectra of reference compounds Sb, Na₃Sb (Sb atoms in green) and NaSb (red and blue atoms identify the two Sb sites).

The ¹²¹Sb Mössbauer spectrum of Sb collected at 78 K was fitted using a quadrupole split component, which provided an isomer shift of $-11.42(3)$ mm s⁻¹ and a small quadrupole splitting of $4.3(8)$ mm s⁻¹, (see Table 1) in agreement with published data and with the slightly distorted octahedral Sb site in Sb metal [24].

The best fit of the spectrum of Na₃Sb gives an isomer shift of $-7.74(4)$ mm s⁻¹ and no quadrupole splitting, in good agreement with calculated IS (δ) of -7.39 mm s⁻¹ and weak QS (Δ) of -1.23 mm s⁻¹ (see Table 2). These results are in line with the high symmetry of the Sb site in the refined structure of Na₃Sb. In this structure, in fact, the Sb atom is at the centre of two interpenetrating Na polyhedra,

a five-fold trigonal bipyramidal and six-fold prism (cf. Figure 1). A small amount of Sb metal impurity (about 10% of the total resonance area) is also detected by ^{121}Sb Mössbauer spectroscopy. In contrast to Sb and Na_3Sb , the structure of NaSb contains two distinct Sb sites. These sites, however, are quite similar: in both of them the Sb atom is at the centre of a distorted polyhedron of 2 Sb and 5 Na atoms. Such complex coordination produces a rather large splitting, which is visible in the Mössbauer spectrum (cf. Figure 1). The fitting provides a QS of $-17.5(4)\text{ mm s}^{-1}$, as well as an IS of $-9.24(6)\text{ mm s}^{-1}$. Also in this case, the Mössbauer spectrum cannot be fitted without including minor amounts of Sb metal, about 15% of the total resonance area. Such minor amounts of Sb metal are actually not detected in the XRD patterns of both intermetallics, indicating that this unreacted Sb is most probably amorphous. This small amount of Sb had only a minor impact on hyperfine parameters as the calculated hyperfine parameters of pure NaSb enabled us to calculate two akin values of IS -8.99 and -9.36 mm s^{-1} and QS of 17.7 and 17.6 mm s^{-1} in line of the experimental result and thus confirming the similarity of the two Sb sites. In short, the two sites of NaSb are so similar that they cannot be discriminated by ^{121}Sb Mössbauer spectroscopy, and the use of a single quadrupole split component with an average isomer shift is largely sufficient to fit its experimental spectrum.

Table 1. ^{121}Sb hyperfine parameters at 78 K for Sb and the Na-Sb intermetallics.

Compound	δ^* [mm s^{-1}]	Δ [mm s^{-1}]	η	Γ [mm s^{-1}]	Area [%]
Sb	$-11.42(2)$	$4.3(8)$	0^{**}	$3.33(1)$	100
Na_3Sb	$-7.74(4)$	0^{**}	0^{**}	$2.85(1)$	$90(2)$
Sb (impurity)	-11.42^{**}	4.3^{**}	0^{**}	3.33^{**}	$10(2)$
NaSb	$-9.24(6)$	$-17.5(4)$	$0.39(8)$	$2.81(8)$	$85(3)$
Sb (impurity)	-11.42^{**}	4.3^{**}	0^{**}	3.33^{**}	$15(3)$

* Isomer shift values are given relative to CaSnO_3 ; ** Values without error were kept fixed during the fitting procedure.

It should be noticed that the robustness of regression procedure regarding the use of several compounds with different Sb environment and oxidation states as well as the fairly good correlation coefficient of 0.98 obtained for the isomer shift and 0.84 for the quadrupole splitting comfort the reliability of the theoretical results. Moreover, the calculated ^{121}Sb quadrupole moment of -67.4 fm^2 agrees well with the previously published value of -66.9 fm^2 , which further corroborates the excellent agreement of experimental data and theoretical calculations [25]. Therefore, and contrarily to previous published results on ^{57}Fe , the B3LYP functional leads to a fairly good correlation even for quadrupole splitting and as good as the classical GGA functional. To the best of our knowledge, this is the first use of hybrid functionals for the extraction of the hyperfine parameters of ^{121}Sb .

Table 2. Calculated ^{121}Sb Mössbauer hyperfine parameters at 0 K for Sb and the Na-Sb intermetallics.

Compound	δ [mm s^{-1}]	Δ [mm s^{-1}]	η
Sb	-11.48	5.6	-1.50
NaSb	-8.99	17.7	0.60
	-9.36	17.6	0.60
$\text{Na}_3\text{Sb-hex}$	-7.39	-1.2	0
$\text{Na}_3\text{Sb-cub}$	-7.56	0	0

In a recent paper by Baggetto et al., two peaks occurring at about -11.2 and -8.0 mm s^{-1} in a spectrum of partially sodiated Sb were attributed to the two Sb lattice sites in the crystal structure of NaSb [8]. On the basis of our findings, however, it is now clear that this interpretation is not correct, and that the two peaks are rather due to a quadrupole split component created by the largely asymmetric coordination of the Sb centres. Taking into account the intrinsic resolution of ^{121}Sb

Mössbauer spectroscopy and the results of the ab initio Mössbauer simulations, it is clear that the high similarity of the coordination environment of the two Sb lattice sites in NaSb makes them virtually indistinguishable in the spectrum.

The EXAFS spectrum of pure antimony can be easily and almost perfectly fitted starting from the well-known structure of Sb metal, using the first 4 Sb-Sb nearest neighbour shells around the Sb centre (cf. Table 3). In this case, relatively low Debye-Waller factors are observed for all shells after the first one. The value of S_0^2 obtained from this fit was used for the fitting of the two Na-Sb intermetallics. The first four nearest neighbour shells were used also in the fitting of NaSb, namely one Sb-Sb shell and three Sb-Na shells. Also in this case, an almost perfect fit is obtained with very high Debye-Waller factors for the three Na-Sb shells. It must be noticed that the small amount of amorphous Sb detected in the ^{121}Sb Mössbauer spectrum of NaSb could not be observed in the EXAFS data. This is likely due to both its low amount and to the very similar Sb-Sb bond length expected for the first coordination shell in both Sb metal and NaSb (cf. Table 3).

Conversely, the EXAFS spectrum of Na_3Sb cannot be fitted by using simply Na-Sb nearest neighbours. In this case, the addition of a noticeable fraction of Sb (slightly less than 20% of the spectrum) is necessary, the Sb-Sb contribution totally dominating in intensity the EXAFS spectrum at high values of k . In addition to this Sb-Sb contribution, the remainder of the spectrum is fitted rather satisfactorily using the first three Sb-Na shells (11 nearest neighbours) typical of the mixed trigonal bipyramidal-prismatic coordination sphere of the Sb centre. The third shell, corresponding to the prismatic coordination, has however a very large Debye-Waller factor, in line with a relatively low-ordered structure.

Table 3. EXAFS fitting parameters for Sb and the Na-Sb intermetallics.

Sample	Shell	N	R_{theo} [Å]	R_{fit} [Å]	σ^2 [Å] ²	S_0^2 *
Sb	Sb-Sb	3	2.908	2.905(2)	0.0055(3)	0.98
	Sb-Sb	3	3.355	3.351(2)	0.017(1)	0.98
	Sb-Sb	6	4.308	4.305(2)	0.017(1)	0.98
	Sb-Sb	6	4.507	4.503(2)	0.017(1)	0.98
NaSb	Sb-Sb	2	2.888	2.852(6)	0.0058(2)	0.98
	Sb-Na	2	3.206	3.261(7)	0.023(5)	0.98
	Sb-Na	1	3.267	3.332(7)	0.023(5)	0.98
	Sb-Na	2	3.322	3.377	0.023(5)	0.98
Na_3Sb (Sb)	Sb-Na	3	3.053	3.04(2)	0.017(2)	0.81(2)
	Sb-Na	2	3.149	3.13(2)	0.017(2)	0.81(2)
	Sb-Na	6	3.428	3.41(2)	0.04(1)	0.81(2)
	Sb-Sb	3	2.908	2.817(8)	0.017(2)	0.17(2)

* Values without error were kept fixed during the fitting procedure.

3.2. The Electrochemical Reaction of Sb with Na: Spectroscopic Results

In our previous work [5], *operando* XRD depicted that the reaction of Na with Sb is accompanied by a general amorphisation, and that the formation of Na_3Sb becomes evident only at the end of the sodiation process. Furthermore, it was shown that two different Na_3Sb polymorphs grow out of the amorphous intermediate which is dominant in the middle of the process, the hexagonal form being commonly obtained from the reaction of the two metals, and a cubic phase known to be stable only at high pressures [29].

The following desodiation of Na_3Sb , on the other hand, produces a totally amorphous phase, XRD becoming totally useless for its identification. This desodiated species can be sodiated again, leading to the gradual reformation of crystallised hexagonal as well as cubic Na_3Sb . It is important to stress that such relatively simple mechanism from the point of view of XRD (one phase disappearing) is characterized by a relatively complicate electrochemical signature: if one looks at its derivative signal, one expects a relatively complex process with at least three intermediate steps [5]. Given the

relatively limited information obtained by XRD due to the general amorphisation of the system, additional local-range techniques, i.e., *operando* XAS and ex situ ^{121}Sb Mössbauer spectroscopy, were employed to better understand the sodiation/desodiation mechanism. Unfortunately, ^{121}Sb Mössbauer spectroscopy cannot be applied in the *operando* configuration due to the relatively high energy of the γ -ray transition of ^{121}Sb , which produces very low Lamb-Mössbauer factors at room temperature for the Sb nuclei in the Sb-containing phases.

The *operando* Sb K-edge XAS spectra (XANES and EXAFS portions) collected during the first three electrochemical processes (sodiation/desodiation/sodiation) are shown in Figure 2 (see Supplementary Materials for the corresponding electrochemical cycling curve.) Even though the absorption edge shifts noticeably during the different electrochemical processes, its features are rather broad and badly defined, and its overall shape varies only slightly. This result is somehow expected, since the very high energy of the absorption K-edge of Sb is connected to a very short lifetime of the core hole, resulting in a low energy resolution of the absorption edge. Consequently, the XANES part (shown in Figure 2a) of the spectrum bears only negligible small information and is hence of little use for the identification of the different species formed during the electrochemical process.

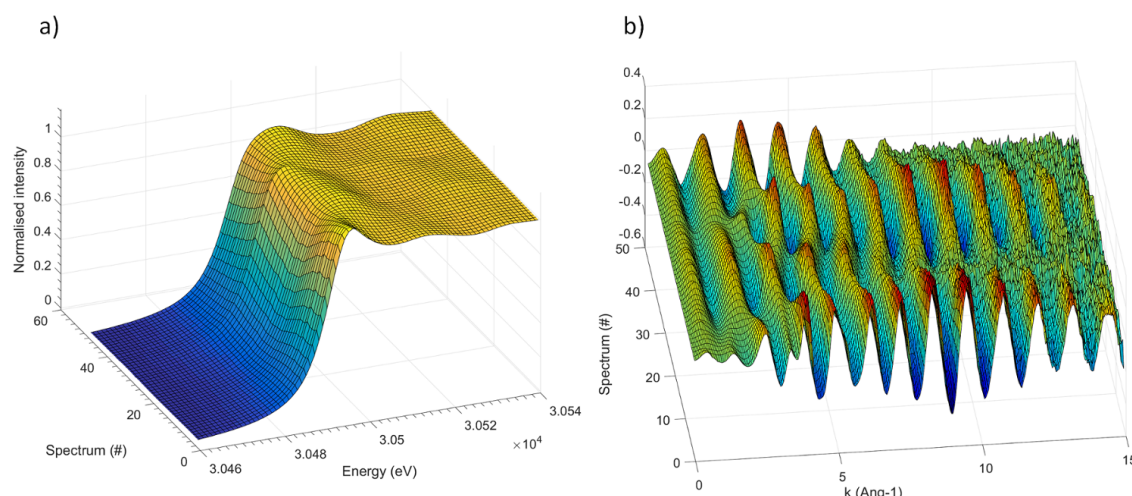


Figure 2. XANES (a) and EXAFS (b) *operando* Sb K-edge spectra measured during the first one and a half electrochemical cycles of Sb electrode vs. Na.

On the other hand, the oscillation of the EXAFS part are rather intense and visible up to $k = 15 \text{ \AA}^{-1}$, and can thus be used to describe the average coordination around the Sb centres. In order to avoid an over-interpretation of the experimental data, and to extract the maximum amount of useful information contained in the *operando* spectra, a principal component analysis (PCA) was performed on the whole set of the EXAFS data. Since the XANES part is varying very little during the process, the differences between the principal components are concentrated in the EXAFS region. The variance plot obtained (Figure 3) shows rather clearly that about 98% of the variance of the EXAFS spectra can be described by three principal components, the residual part can be attributed to the experimental noise. A visualisation of the shape of the principal components and of the respective scores (see details in the Supplementary Materials) support this hypothesis, with both shape and evolution of the first three components varying gradually through the different processes, and those of the following ones changing in a totally hectic way.

Even though the so-obtained principal components are only orthogonal mathematical functions and not real EXAFS spectra, their determination reveals the number of independent spectral components that can be used to fit the whole set of experimental data. Several methodologies are then available to reconstruct the corresponding real EXAFS components as well as their evolution. In this case, the MCR-ALS analysis was used [18,19] producing the three EXAFS spectra shown in

Figure 4 together with their evolution along the different electrochemical processes. These components correspond perfectly to specific spectra measured along the in situ measurements, in line with their observed evolution (see also Supplementary Materials section): component 1, for instance, is practically identical to the spectrum of pristine Sb. On the other hand, component 2 resembles perfectly the spectrum obtained at the end of the charge process, corresponding to the fully desodiated electrode, whereas component 3 is identical to spectrum obtained at the end of the first discharge, i.e., to full sodiation.

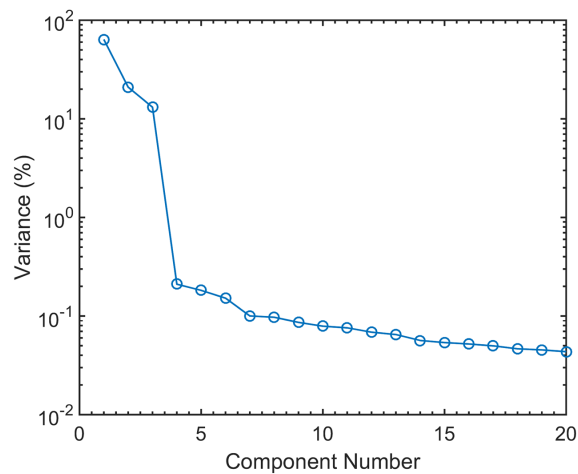


Figure 3. Variance plot obtained by the Principal Component Analysis of EXAFS *operando* spectra. Three components containing almost 98% of total spectra information stand out, the residuals represent the experimental noise.

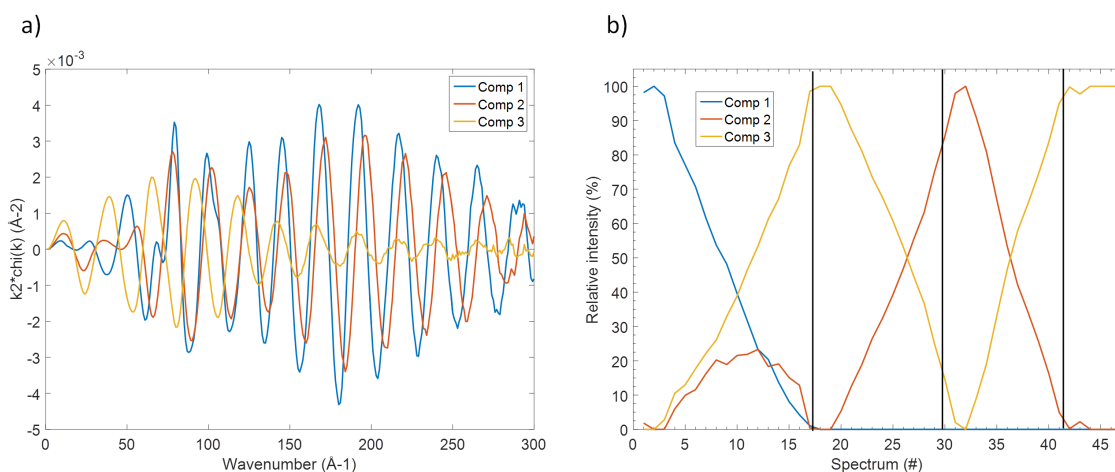


Figure 4. EXAFS spectral components (a) obtained by MCR-ALS analysis of the EXAFS *operando* spectra, and variation of their intensity (b) during electrochemical cycling. The vertical black lines represent the end of each process (first discharge, first charge, and second discharge).

These reconstructed spectra were then fitted in the traditional way, starting from the known structures of Sb metal and hexagonal Na₃Sb (vide supra). The results of the fit are reported in Table 4. While the fitting of Component 1 is trivial and identical to that of pristine Sb presented above, Component 2 can be fitted by using solely the first coordination shells of Sb metal, with a significant decrease of the average Sb-Sb distance and of the coordination number but without noticeably varying the Debye-Waller factor. The presence of only one tri-coordinated Sb-Sb shell with a Sb-Sb interatomic distance lower than in Sb metal bears resemblance to the long known structure of the

amorphous “explosive antimony”, synthesised by Krebs et al. by electrolysis of antimony chloride [30]. The proposed structural model for this phase is based on a disordered network of antimony, where all antimony atoms are bonded to three other ones with a Sb-Sb distance sensibly lower than in Sb metal. A large range of coordination angles results in the total disappearance of the spectral contributions beyond the first nearest neighbour shell, and hence of the long-range order. It is important to notice that such interpretation is complete agreement with the totally flat X-ray diffraction pattern observed at the end of the charge process. Finally, the fitting of Component 3 can be performed using the first two Sb-Na shells of hexagonal Na₃Sb, as well as a minor contribution from a Sb-Sb shell at short distances, probably due to the presence of some residual unreacted Sb metal.

Table 4. EXAFS fitting parameters for the reconstructed MCR components.

Component	Shell	N	R _{theo} [Å]	R _{fit} [Å]	σ ² [Å] ²	S ₀ ² *
1	Sb-Sb	3	2.908	2.905(2)	0.0055(3)	0.98
	Sb-Sb	3	3.355	3.351(2)	0.017(1)	0.98
	Sb-Sb	6	4.308	4.305(2)	0.017(1)	0.98
	Sb-Sb	6	4.507	4.503(2)	0.017(1)	0.98
2	Sb-Sb	3	2.908	2.850(2)	0.0061(3)	0.98
3	Sb-Sb	3	2.908	2.885(9)	0.09(4)	0.09(4)
	Sb-Na	3	3.053	3.052(8)	0.016(1)	0.89(4)
	Sb-Na	2	3.149	3.122(8)	0.016(1)	0.89(4)

* Values without error were kept fixed during the fitting procedure.

With these spectral information in mind, it is now possible to follow the evolution of these different phases during the different sodiation/desodiation/sodiation processes shown in Figure 4b. In fact, not only pristine Sb metal is gradually transformed into Na₃Sb during the first discharge, but simultaneously some amorphous Sb appears too, in line with the gradual amorphisation of the system during the reaction with Na. Almost pure Na₃Sb is obtained at the end of sodiation, and during the following charge, this phase is desodiated leading to amorphous Sb metal. This phase is then reversibly sodiated/desodiated during the following discharge/charge cycles.

However, it is important to notice that, with the exception of the amorphisation of Sb during the first sodiation (which might occur with the insertion of some Na in the Sb lattice), these analyses could not evidence the formation of any intermediate Na-Sb species. This result is somehow in contradiction not only with the work of Baggetto et al. [9], who suggested the formation of an amorphous form of NaSb as an intermediate phase during the discharge, but also with more recent results that we obtained by *operando* PDF and ex situ ²³Na Solid State NMR analysis [7]. In that work, two different electrochemically formed intermediates could be identified: (i) amorphous Na_{3-x}Sb (with x ≈ 0.4–0.5), having a local structure similar to crystalline Na₃Sb but with a significant number of sodium vacancies and a limited correlation length, and (ii) amorphous Na_{1.7}Sb, with a highly amorphous structure featuring some Sb-Sb bonding. Even though the first of these two phases seem to form during the first sodiation, the second one is expected to appear only during the following desodiation. It is important to notice that such phases, even though mostly amorphous, can be identified by PDF in the direct space using the series of peaks from 2 to about 10 Å. Contrary to PDF, in the EXAFS spectra measured during the *operando* processes, only the first coordination shells are visible due to the amorphous nature of the samples, with the notable exception of pristine Sb where also the second coordination shell is visible. This limit of EXAFS compared to PDF is inherent to the nature of the probe: scattered electrons and X-rays in EXAFS and PDF, respectively, which have different diffusion path lengths in the materials. Therefore, even though EXAFS is more sensitive to the nature of the neighbouring atoms, and Sb atoms can thus be distinguished from the Na ones in the fits, the analysis remains restricted to the neighbours corresponding to only the first peak of the PDF signal, and is thus not sufficient to differentiate among the variety of possible amorphous phases.

As an example to outline this difficulty in identifying possible intermediate phases, one can compare the first coordination shell of the spectrum of crystalline NaSb (prepared by ball milling as a reference, *vide supra*) with that observed for spectrum #33 of the *operando* spectra series, corresponding to the reaction of about 1 mol Na during second discharge. The two EXAFS spectra, shown in Figure 5, are almost identical, and this similarity becomes more evident if one looks at the Fourier transform of the two spectra, which are practically identical in both the envelope and the imaginary part of the function. Considering that the *operando* spectrum can be obtained by a simple linear combination of the second and the third components issued from the MCR-ALS analysis, corresponding to amorphous antimony and Na₃Sb, respectively, it is clear that the possible formation of NaSb is impossible to spot in the whole series of spectra. The similarity of the two spectra is on the other hand not surprising, since the first Sb-Na and Sb-Sb coordination shells in Na₃Sb and amorphous Sb have similar bond distances to those in the structure of NaSb, and an appropriate ratio of the two phases would correspond to the expected ratio in NaSb. Since similar conclusion can be drawn for the other possible expected intermediates, it is clear that no conclusive information about the possible formation of intermediates during the electrochemical reaction of Sb with Na can be obtained by EXAFS.

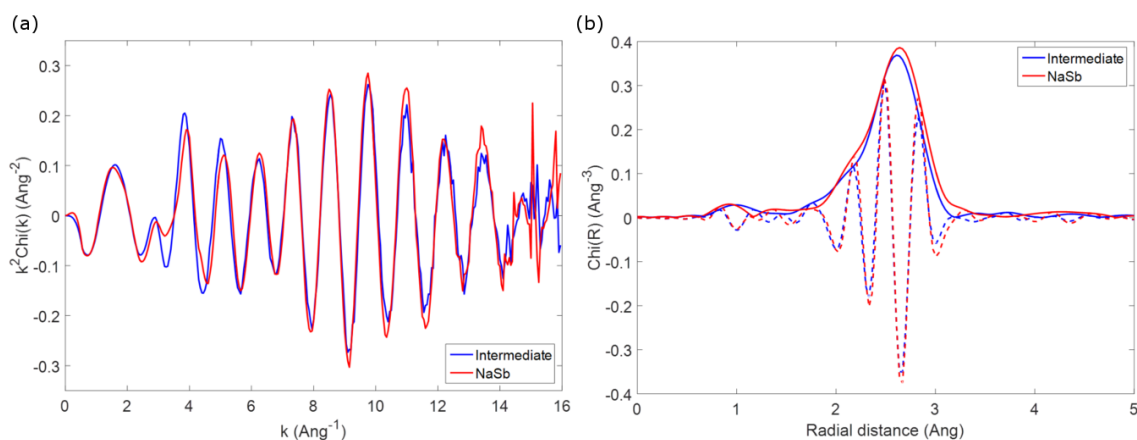


Figure 5. EXAFS spectra (a) and respective Fourier Transform (b) of NaSb (red) and of the Sb electrode after the reaction of about 1 mol Na per mol of Sb during the second discharge (blue).

Similar problems concerning the identification of possible intermediates arise also from the analysis of ex situ ¹²¹Sb Mössbauer spectra. The Mössbauer spectra of two Sb electrodes collected at the end of first discharge and at the end of the first charge, and of two additional electrodes stopped after the reaction of 1.5 and 2 mol of Na per mol of Sb during the first discharge, are shown in Figure 6. The interpretation of the Mössbauer spectra of the first two electrodes is rather straightforward: (i) the spectrum of the fully discharged sample is practically identical to that of pure Na₃Sb (cf. Tables 1 and 5), in line with the full sodiation of the starting antimony, whereas (ii) the spectrum of the fully charged sample is only slightly different from that of the starting antimony. In fact, in addition to a minor impurity of unreacted Na₃Sb, the dominant component of the latter spectrum has an isomer shift slightly more positive than that of bulk antimony. This difference can be simply explained either by an incomplete desodiation of the antimony, or more likely by the formation of amorphous Sb, which has a slightly different coordination shell compared to bulk antimony, as testified by both the EXAFS results and the previously published XRD and PDF analyses [5,7].

The interpretation of the two intermediate spectra, however, is not so straightforward. For simplicity, they were first fitted with two spectral components, as shown in Figure 6, with the parameters reported in Table 5. Using the results of this fitting, one obtains, after the reaction of 1.5 Na, i.e., halfway through first discharge, the presence of half Na₃Sb and half amorphous Sb. After the reaction of 2.0 Na, i.e., at two thirds of the first discharge, the spectral component of Na₃Sb represents about two thirds of the spectrum, whereas the remaining one third is represented by a component

with an isomer shift significantly more positive than those of both bulk and amorphous Sb. The latter component could be interpreted with the presence of a sort of amorphous Sb containing some Na. For both samples, the relative intensities of the two observed components would follow well the stoichiometry of the system, thus supporting this interpretation. The possible presence of intermediate phases, however, is virtually impossible to distinguish from the simultaneous presence of Na_3Sb and amorphous Sb. In fact, species such as NaSb would give rise to quadrupole split components (cf. Table 1 and Figure 1) with a global shape that resembles the sum of the two components representing Na_3Sb and amorphous Sb. Consequently NaSb would be thus completely disguised by their signals.

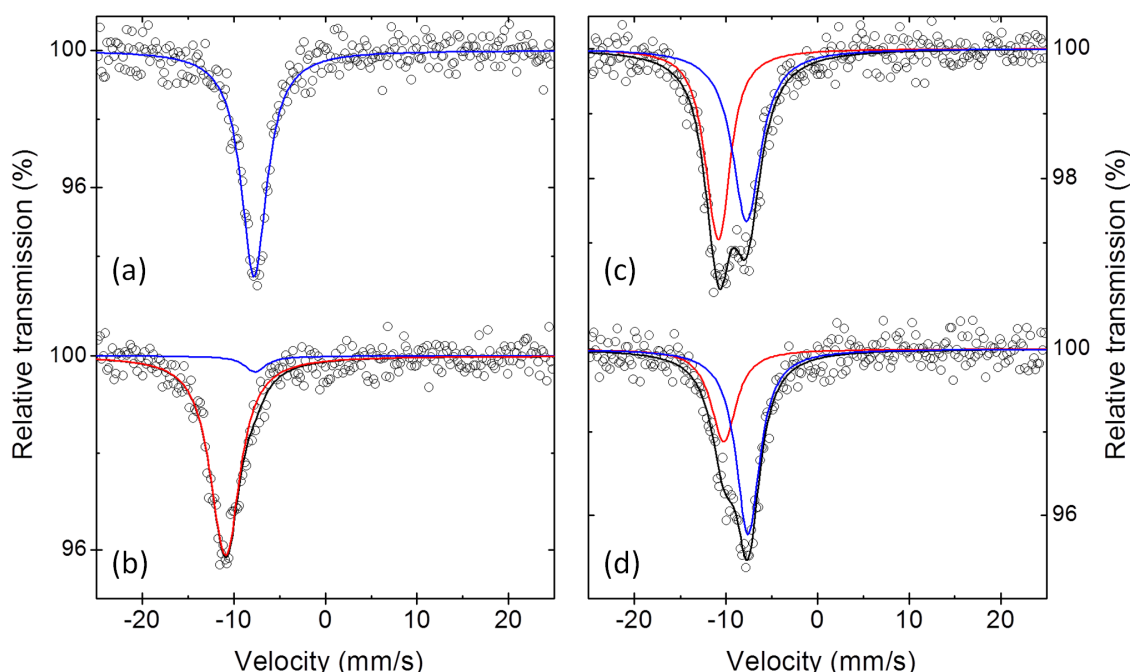


Figure 6. ^{121}Sb Mössbauer spectra at 78 K of Sb electrodes at the end of first discharge (a), at the end of first charge (b), after the reaction of 1.5 mol Na during first discharge (c) and after reaction of 2 mol Na during the first discharge (d).

It is interesting to notice that Baggetto et al. proposed the formation of NaSb during the electrochemical sodiation of Sb on the basis of such an ambiguous spectrum [8]. On the basis of our results, however, it is now clear that such an interpretation is not at all unequivocal, and that the possible formation of NaSb is difficult to differentiate by ^{121}Sb Mössbauer spectroscopy from the simultaneous presence of Na_3Sb and amorphous Sb. This ambiguity might be resolved, perhaps, by combining ^{121}Sb Mössbauer spectroscopy with synchrotron radiation Nuclear Forward Scattering, which has better resolution [31].

In summary, both EXAFS ^{121}Sb Mössbauer spectroscopy support the formation of Na_3Sb after full sodiation and of amorphous Sb after desodiation, in line with the previously published results. However, even applied together, these two techniques appear as intrinsically unable to spot the possible formation of intermediate Na-Sb phases during the electrochemical cycling of Sb vs. Na. Until today, only the simultaneous application of PDF and ^{23}Na Solid State NMR spectroscopy have allowed the unequivocal determination of the formation of such intermediates [7].

Table 5. Ex situ ^{121}Sb hyperfine parameters at 78 K for the cycled Sb electrodes.

Sample	δ^* [mm s^{-1}]	Δ [mm s^{-1}]	η	Γ [mm s^{-1}]	Area [%]
EOD 1st cycle	−7.68(4)	0	0 **	2.8(1)	100
EOC 1st cycle	−10.96(8)	4.5(6)	0 **	3.5(5)	94(3)
	−7.68 **	0 **	0 **	2.8 **	6(3)
1st disch. 1.5 Na reacted	−10.91(8)	4.7(8)	0 **	2.8(3)	52(2)
	7.81(1)	0 **	0 **	3.6(6)	48(5)
1st disch. 2 Na reacted	−10.4(2)	4.7(8)	0 **	2.6(5)	30(6)
	−7.65(8)	0 **	0 **	3.2(6)	70(6)

* Isomer shift values are given relative to CaSnO_3 ; ** Kept fixed during the fitting procedure.

4. Conclusions

The application of *operando* XAS and Mössbauer spectroscopy for investigating the sodiation mechanism of Sb, supported by ab initio DFT calculation, shows that during first sodiation a gradual transformation of Sb into disordered Na_3Sb occurs along with simultaneous amorphisation of Sb. Upon charge inversion, the Na_3Sb is progressively transformed into amorphous Sb, which is distinct from pristine Sb. In subsequent second discharge this amorphous Sb is gradually transformed to disordered Na_3Sb .

The formation of Na-Sb intermediate phases could not be evidenced since such intermediates cannot be distinguished from intermediate compositions by XAS. On the other hand, the use of DFT was helpful for the determination of the hyperfine parameters of the Mössbauer spectra of the pure Na-Sb phases, showing that an unambiguous attribution of the measured hyperfine spectra is virtually impossible without further support by complementary techniques.

Supplementary Materials: The following are available online at www.mdpi.com/2313-0105/4/2/25/s1.

Author Contributions: L.S., M.T.S. and L.M. conceived and designed the experiments with the help of C.L.F. and A.D.; A.D., A.M., B.F. and M.T.S. prepared the materials and performed the experiments; L.S., A.D. and M.T.S. analyzed the data; M.B.Y. performed the ab initio calculation; L.S., L.M., R.P.H. and M.-L.D. supervised the study; L.S., M.F. and M.B.Y. wrote the paper; all authors helped in editing and correcting the manuscript until its final version.

Acknowledgments: S. Belin and V. Briois are gratefully acknowledged for their expert advice on beamline operation, Synchrotron Soleil (France) for providing beamtime at the beamline SAMBA. Alistore-European Research Institute is gratefully acknowledged for financial support through the postdoc grants to A.D. and M.F. Work by R.P.H. was sponsored by UT-Battelle, LLC under Contract No. DE-AC05-00OR22725 with the U.S. Department of Energy. The research group *Catalyse, Réactivité de Surface et Rayonnement Synchrotron* (GDR CNRS 3590) is gratefully acknowledged for its information and supporting activity for the application of the chemometric approach in the analysis of spectroscopic data.

Conflicts of Interest: The authors declare no conflict of interest.

Abbreviations

The following abbreviations are used in this manuscript:

XAS	X-ray Absorption spectroscopy
EXAFS	Extended X-ray Absorption Fine Structure
XANES	X-ray Absorption Near-Edge Structure
XRD	X-ray Diffraction
PDF	Pair Distribution Function
PCA	Principal Component Analysis
MCR-ALS	Multivariate Curve Resolution-Alternating Least Squares
DFT	Density Functional Theory
NMR	Nuclear Magnetic Resonance

References

1. Tarascon, J.M. Is lithium the new gold? *Nat. Chem.* **2010**, *2*, 510. [[CrossRef](#)] [[PubMed](#)]
2. Kawamoto, H.; Tamaki, W. Trends in Supply of Lithium Resources and Demand of the Resources for Automobiles. *Sci. Technol. Trends Quart. Rev.* **2011**, *369*, 51–64.
3. Fang, Y.; Chen, Z.; Xiao, L.; Ai, X.; Cao, Y.; Yang, H. Recent Progress in Iron-Based Electrode Materials for Grid-Scale Sodium-Ion Batteries. *Small* **2018**, *14*, 1703116. [[CrossRef](#)] [[PubMed](#)]
4. He, J.; Wei, Y.; Zhai, T.; Li, H. Antimony-based materials as promising anodes for rechargeable lithium-ion and sodium- ion batteries. *Mater. Chem. Front.* **2018**, *2*, 437–455. [[CrossRef](#)]
5. Darwiche, A.; Marino, C.; Sougrati, M.T.; Fraisse, B.; Stievano, L.; Monconduit, L. Better cycling performances of bulk Sb in Na-ion batteries compared to Li-ion systems: An unexpected electrochemical mechanism. *J. Am. Chem. Soc.* **2012**, *134*, 20805–20811. [[CrossRef](#)] [[PubMed](#)]
6. Saubanère, M.; Ben Yahia, M.; Lemoigno, F.; Doublet, M.L. Influence of polymorphism on the electrochemical behavior of MxSb negative electrodes in Li/Na batteries. *J. Power Sources* **2015**, *208*, 695–702. [[CrossRef](#)]
7. Allan, P.K.; Griffin, J.M.; Darwiche, A.; Borkiewicz, O.J.; Wiaderek, K.M.; Chapman, K.W.; Morris, A.J.; Chupas, P.J.; Monconduit, L.; Grey, C.P. Tracking Sodium-Antimonide Phase Transformations in Sodium-Ion Anodes: Insights from Operando Pair Distribution Function Analysis and Solid-State NMR Spectroscopy. *J. Am. Chem. Soc.* **2016**, *138*, 2352–2365. [[CrossRef](#)] [[PubMed](#)]
8. Baggetto, L.; Hah, H.Y.; Jumas, J.C.; Johnson, C.E.; Johnson, J.A.; Keum, J.K.; Bridges, C.A.; Veith, G.M. The reaction mechanism of SnSb and Sb thin film anodes for Na-ion batteries studied by X-ray diffraction, ^{119}Sn and ^{121}Sb Mössbauer spectroscopies. *J. Power Sources* **2014**, *267*, 329–336. [[CrossRef](#)]
9. Baggetto, L.; Ganesh, P.; Sun, C.N.; Meisner, R.A.; Zawodzinski, T.A.; Veith, G.M. Intrinsic thermodynamic and kinetic properties of Sb electrodes for Li-ion and Na-ion batteries: Experiment and theory. *J. Mater. Chem. A* **2013**, *1*, 7985. [[CrossRef](#)]
10. Cromer, D.T. The crystal structure of NaSb. *Acta Crystallogr.* **1959**, *12*, 41–45. [[CrossRef](#)]
11. Brauer, G. *Handbook of Preparative Inorganic Chemistry V1*; Academic Press: New York, NY, USA, 1963; p. 1031.
12. Frontera, C.; Rodríguez-Carvajal, J. FullProf as a new tool for flipping ratio analysis. *Phys. B Condens. Matter* **2003**, *335*, 219–222. [[CrossRef](#)]
13. Grosse, G. *PC-Mos II, Version 1.0 Manual and Program Documentation*; Technische Universität München: Munich, Germany, 1993.
14. Leriche, J.B.; Hamelet, S.; Shu, J.; Morcrette, M.; Masquelier, C.; Ouvrard, G.; Zerrouki, M.; Soudan, P.; Belin, S.; Elkaïm, E.; et al. An electrochemical cell for operando study of lithium batteries using synchrotron radiation. *J. Electrochem. Soc.* **2010**, *157*, A606–A610. [[CrossRef](#)]
15. Ravel, B.; Newville, M. ATHENA, ARTEMIS, HEPHAESTUS: Data analysis for X-ray absorption spectroscopy using IFEFFIT. *J. Synchrotron Radiat.* **2005**, *12*, 537–541. [[CrossRef](#)] [[PubMed](#)]
16. Ankudinov, A.; Rehr, J. Relativistic calculations of spin-dependent x-ray-absorption spectra. *Phys. Rev. B Condens. Matter Mater. Phys.* **1997**, *56*, R1712–R1716. [[CrossRef](#)]
17. Massart, D.; Vandeginste, B.; Buydens, L.; De Jong, S.; Lewi, P.; Smeyers-Verbeke, J. *Handbook of Chemometrics and Qualimetrics: Part A*, 1st ed.; Elsevier: Amsterdam, The Netherlands, 1997.
18. Jaumot, J.; Gargallo, R.; De Juan, A.; Tauler, R. A graphical user-friendly interface for MCR-ALS: A new tool for multivariate curve resolution in MATLAB. *Chemom. Intell. Lab. Syst.* **2005**, *76*, 101–110. [[CrossRef](#)]
19. Jaumot, J.; de Juan, A.; Tauler, R. MCR-ALS GUI 2.0: New features and applications. *Chemom. Intell. Lab. Syst.* **2015**, *140*, 1–12. [[CrossRef](#)]
20. Dovesi, R.; Orlando, R.; Erba, A.; Zicovich-Wilson, C.M.; Civalleri, B.; Casassa, S.; Maschio, L.; Ferrabone, M.; La Pierre, M.D.; D'Arco, P.; et al. CRYSTAL14: A program for the ab initio investigation of crystalline solids. *Int. J. Quantum Chem.* **2014**, pp. 1287–1317. [[CrossRef](#)]
21. Dovesi, R.; Saunders, V.R.; Roetti, C.; Orlando, R.; Zicovich-Wilson, C.; Pascale, F.; Civalleri, B.; Doll, K.; Harrison, N.M.; Bush, I.J.; et al. *CRYSTAL 2014 User's Manual*; University of Torino: Torino, Italy, 2014.
22. Becke, A. Density—Functional thermochemistry. III. The role of exact exchange. *J. Chem. Phys.* **1993**, *98*, 5648. [[CrossRef](#)]
23. Lee, C.; Yang, W.; Parr, R. Development of the Colle-Salvetti correlation-energy formula into a functional of the electron density. *Phys. Rev. B Condens. Matter* **1988**, *37*, 785. [[CrossRef](#)] [[PubMed](#)]

24. Lippens, P.E. Mössbauer isomer shifts of crystalline antimony compounds. *Solid State Commun.* **2000**, *113*, 399–403. [[CrossRef](#)]
25. Svane, A. Calculations of hyperfine parameters in antimony compounds. *Phys. Rev. B* **2003**, *68*, 064422. [[CrossRef](#)]
26. Casassa, S.; Ferrari, N.M. Calibration of ^{57}Fe Mössbauer constants by first principles. *Phys. Chem. Chem. Phys.* **2016**, *18*, 10201–10206. [[CrossRef](#)] [[PubMed](#)]
27. Brauer, G.Z.E. Konstitution von Phosphiden, Arseniden, Antimoniden und Wismutiden des Lithiums, Natriums und Kaliums. *Z. Phys. Chem.* **1937**, *37*, 323–352. [[CrossRef](#)]
28. Songster, J.; Pelton, A.D. The Na-Sb (sodium-antimony) system. *J. Phase Equilib.* **1993**, *14*, 250–255. [[CrossRef](#)]
29. Leonova, M.E.; Bdikin, I.K.; Kulinich, S.A.; Gulish, O.K.; Sevast'yanova, L.G.; Burdina, K.P. High-pressure phase transition of hexagonal alkali pnictides. *Inorg. Mater.* **2003**, *39*, 266–270. [[CrossRef](#)]
30. Krebs, H.; Steffen, R. Neubestimmung der Nahordnung im glasigen Selen, im explosiven Antimon und im beta- und gamma-Arsen. *Z. Anorg. Allg. Chem.* **1964**, *327*, 224–237. [[CrossRef](#)]
31. Sergueev, I.; Wille, H.C.; Hermann, R.P.; Bessas, D.; Shvyd'ko, Y.V.; Zajac, M.; Rüffer, R. Milli-electronvolt monochromatization of hard X-rays with a sapphire backscattering monochromator. *J. Synchrotron Radiat.* **2011**, *18*, 802–810. [[CrossRef](#)] [[PubMed](#)]



© 2018 by the authors. Licensee MDPI, Basel, Switzerland. This article is an open access article distributed under the terms and conditions of the Creative Commons Attribution (CC BY) license (<http://creativecommons.org/licenses/by/4.0/>).